Tsunami Potential of Moderate Earthquakes: The July 1, 2009 Earthquake (M_w 6.45) and its Associated Local Tsunami in the Hellenic Arc

GIAN MARIA BOCCHINI,[1,3] T. NOVIKOVA,[1] G. A. PAPADOPOULOS,[1] A. AGALOS,[1] E. MOUZAKIOTIS,[1] V. KARASTATHIS,[1] and N. VOULGARIS[2]

Abstract—On July 1, 2009, a M_w 6.45 earthquake ruptured south of Crete Island (Greece) along the Hellenic Arc triggering a local tsunami. Eyewitness reported the tsunami from Myrtos and Arvi (south-eastern Crete) and from the north of Chrisi Islet, located to the southeast of Crete. The earthquake occurred offshore, about 80 km south of Crete, where routine earthquake locations are poor. The hypocentre is relocated using a 2-D velocity model and several local 1-D velocity models. Epicentral locations obtained by using the different velocity models show very minor variations. Instead, relocated hypocentres can be grouped into two sets of solutions: (1) those with a shallower depth (depth < 12 km) obtained with the 2-D velocity model and the 1-D velocity models having a shallower Moho at less than 30 km, and (2) those with a larger depth (depth of 28 and 40 km) obtained with the velocity models having a Moho at about 40 km. Shallower hypocentres are more consistent with the tsunamigenic nature of the earthquake as also supported by tsunami numerical simulations. In fact, shallow sources (depths < 12 km) are capable of generating tsunami waves, while it is not the case for deeper sources (depth > 25 km) either in the upper-plate or along the plate interface. Models accounting for either homogeneous or heterogeneous slip on the causative fault are tested, with the heterogeneous one better reproducing the observations in terms of number of tsunami waves reaching the shoreline and duration of the sea disturbance. The short travel time, about 10 min, of the first tsunami arrival at the southern coast of Crete represents a big challenge for tsunami early warning systems operating in the area.

Key words: Hellenic subduction zone, tsunamigenic earthquakes, tsunami hazard, earthquake relocation, tsunami early warning systems.

[1] Institute of Geodynamics, National Observatory of Athens, Lofos Nymfon 1, 11810 Athens, Greece. E-mail: bocchini@noa.gr; Gian.Bocchini@rub.de

[2] Department of Geology and Geoenvironment, National and Kapodistrian University of Athens, Athens, Greece.

[3] Faculty of Geosciences, Institute of Geology, Mineralogy, and Geophysics, Ruhr University of Bochum, Bochum, Germany.

1. Introduction

The Hellenic subduction zone (HSZ; Fig. 1) is seismically the most active structure in the eastern Mediterranean Sea. The high seismicity is associated with the convergence between the Nubian Plate and the Aegean region occurring at about 35–40 mm/year (McClusky et al. 2000; Reilinger et al. 2006).

Historical and instrumental seismicity catalogues for Greece, covering more than 2000 years (e.g., Guidoboni and Comastri 2005; Papazachos and Papazachou 2003; Ambraseys 2009), report the occurrence of several large earthquakes of magnitude larger than 7. At least two earthquakes with estimated magnitude larger than 8, namely the 365 CE and the 1303 CE ones, ruptured the western and eastern segments of the HSZ, respectively (Guidoboni and Comastri 1997; Shaw et al. 2008; Papadopoulos 2011). These two earthquakes triggered large tsunamis that inundated many coastal localities in the entire basin of the eastern Mediterranean causing loss of life and devastation (Papadopoulos 2011; Papadopoulos et al. 2014). The largest documented earthquake and associated tsunami occurred in the HSZ, namely the 365 CE ($M \sim 8.3$) event, very likely ruptured the overriding plate southwest of Crete and not the main plate interface as would be expected for such large earthquakes in a subduction zone (Shaw et al. 2008). More recently, a destructive tsunami was also generated by the surface wave magnitude (M_s) 7.4 normal faulting earthquake of the 9th of July 1956 that occurred in the back-arc area (Fig. 1; Galanopoulos 1957). The high seismogenic and tsunamigenic hazard associated with the active margin to the south of Crete, as highlighted by
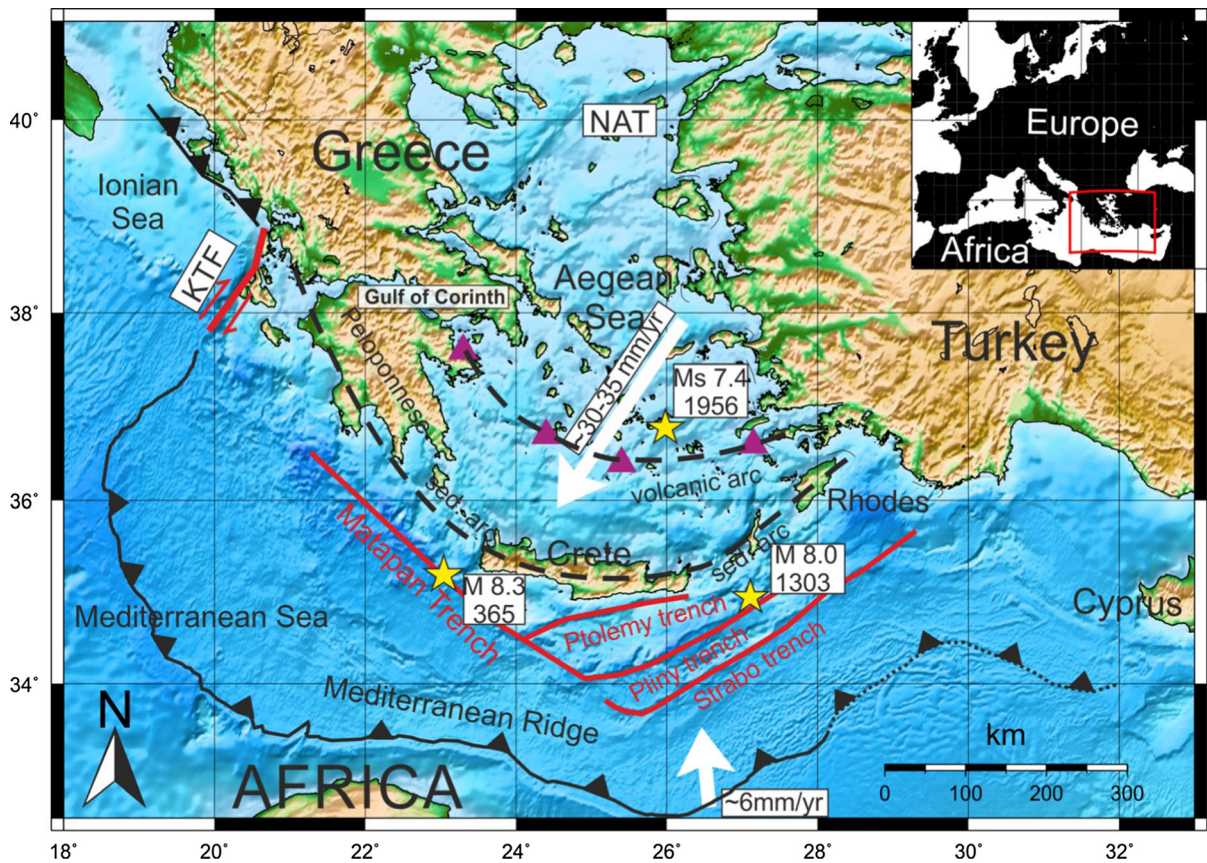
Figure 1
Map view of the Hellenic subduction zone. Line with triangles (in black) indicates the deformation front. Yellow stars indicate the epicentral location of some of the largest tsunamigenic earthquakes that have occurred in the Aegean region, namely the $M \sim 8.3$ 365 CE, the $M \sim 8$ 1303 CE and the more recent M_s 7.4 1956 Amorgos earthquakes (see text for references). White arrows indicate the motion of the Nubian Plate (lower) and of the Aegean region (upper) with respect to the stable Eurasian Plate. The purple triangles in the central Aegean indicate the position of the volcanic arc. *KTF* Kefalonia Transform Fault; *NAT* North Aegean Trough; *sed. arc* sedimentary arc

historical and instrumental records (Papadopoulos 2011), poses interest in the study of seismogenic and tsunamigenic sources in the area.

On July 1, 2009, UTC 09:30, a moderate magnitude earthquake of moment magnitude (M_w) 6.45 ruptured the southern offshore margin of Crete (Fig. 3) causing a local tsunami of about 0.3 m in height, as reported by eyewitnesses. This earthquake provided a good opportunity to further investigate the seismogenic and tsunamigenic sources in the HSZ and particularly the south of Crete segment. We used various velocity models to relocate the event, while tsunami numerical simulations were performed for different fault scenarios reproducing the different locations obtained. Synthetic and observed tsunami waves were compared aiming to constrain the best fault solution. Moreover, the implications for the seismogenic and tsunamigenic potential in the area are discussed. Yet, although of moderate magnitude and not damaging, the study of such kind of earthquakes is very useful for testing the performance of early warning systems in the Mediterranean Sea.

2. Geotectonic Setting and Seismic Imaging

The forearc and the inter-plate seismogenic zone in the area of Crete have been widely investigated through temporary local seismic networks (e.g., Delibasis et al. 1999; Meier et al. 2004; Becker et al.

2010) and active seismic experiments (e.g., Bohnhoff et al. 2001). To the south of Crete, strong micro-seismicity occurs along the subduction plate interface from about 20 to 40-km depth and in the upper crust mainly along morphotectonic features, namely the Ptolemy, Pliny and Strabo trenches (e.g., Delibasis et al. 1999; Meier et al. 2004; Becker et al. 2010).

Eurasia-Africa convergence at the HSZ is accommodated by low-angle thrust faults (dip angles < 20°), dipping towards the volcanic arc, that are located at depths between about 15 and 45 km along the subduction plate interface (e.g., Taymaz et al. 1990; Kiratzi and Louvari 2003; Shaw and Jackson 2010; Fig. 1). Higher-angle reverse faults with dip angles larger than 30°, also dipping towards the volcanic arc, are located at shallower depths, between about 5 and 30 km, and have been suggested to splay off from the main plate interface (Taymaz et al. 1990; Shaw and Jackson 2010). Repeated activity along such a high-angle reverse fault has been proposed to produce pronounced bathymetric features on the ocean floor (Shaw et al. 2008; Mouslopoulou et al. 2015).

The accuracy of earthquake locations is of crucial importance for reliably constraining seismic sources. Routine earthquake locations in the outer forearc, where most of the seismicity occurs (Fig. 2), are usually poor due to the low station density along the sedimentary arc, the poor azimuthal coverage, and the presence of a velocity structure hardly reproduced by the simple 1-D velocity models used. Sachpazi et al. (2016) compared locations obtained by a local network composed by ocean bottom seismometers (OBSs) and land stations with those obtained from the National Observatory of Athens (NOA, http://bbnet.gein.noa.gr/HL/) in the outer forearc, between southern Peloponnese and western Crete. The study revealed errors up to several tens of kilometres in the revised seismicity catalogue of NOA. Karastathis et al. (2015) showed how the adoption of a 2-D velocity model, resembling the upper crust thickening from the plate boundary towards the inner forearc, significantly improved the location accuracy and the spatial distribution of the seismicity in the area of the Kefalonia Transform Fault, when compared to the revised hypocentral solutions from NOA. In fact, a crustal thickness variation of more than 10 km

corresponds to additional travel times of up to 1 s, leading to location errors up to several tens of kilometres if not taken into account in the location algorithms (Koulakov and Sobolev 2006).

Results from a wide-angle seismic experiment along three profiles onshore and offshore of Crete showed that the lateral variation of the crustal and sedimentary thickness is stronger along the N–S direction than along the E–W direction (Bohnhoff et al. 2001). A maximum crustal thickness of about 32.5 km is observed to the north of central Crete and decreases to 28–30 km towards west and to 24–26 km towards east (Bohnhoff et al. 2001). North of Crete the crust thins to about 15 km below the Cretan Sea and to the south it reaches about 17 km at the plate boundary, located approximately 100 km south of Crete below the Mediterranean Ridge (Bohnhoff et al. 2001; Fig. 1). The crustal thickness beneath Crete, inferred by wide-angle seismic data, is consistent with results from other independent geophysical studies based on receiver function techniques (e.g., Li et al. 2003; Sodoudi et al. 2006) or combined seismic and gravimetric data (e.g., Makris et al. 2013).

3. The July 1, 2009 Earthquake

The M_w 6.45 July 1, 2009 earthquake struck offshore, about 80 km to the south of Crete (Fig. 3), where hypocentral coordinates are poorly constrained, as discussed in the introduction. The shock was slightly felt in several places of Crete and as far as Cairo in Egypt and Nicosia in Cyprus.

NOA, the official agency providing real-time earthquake solutions in Greece, calculated an epicentre at 34.35N/25.40E and a focal depth of 30 km. Different locations were obtained from the European Mediterranean Seismological Centre (EMSC), which calculated an epicentre at 34.14N/25.42E and a focal depth of 30 km, and by the International Seismological Centre (ISC), which calculated an epicentre at 34.15N/25.54E and a focal depth of 13.7 km. The three aforementioned solutions show a maximum difference of about 30 km in epicentral coordinates and 16 km in focal depth. The discrepancy in hypocentral coordinates can be inferred to: (1) the
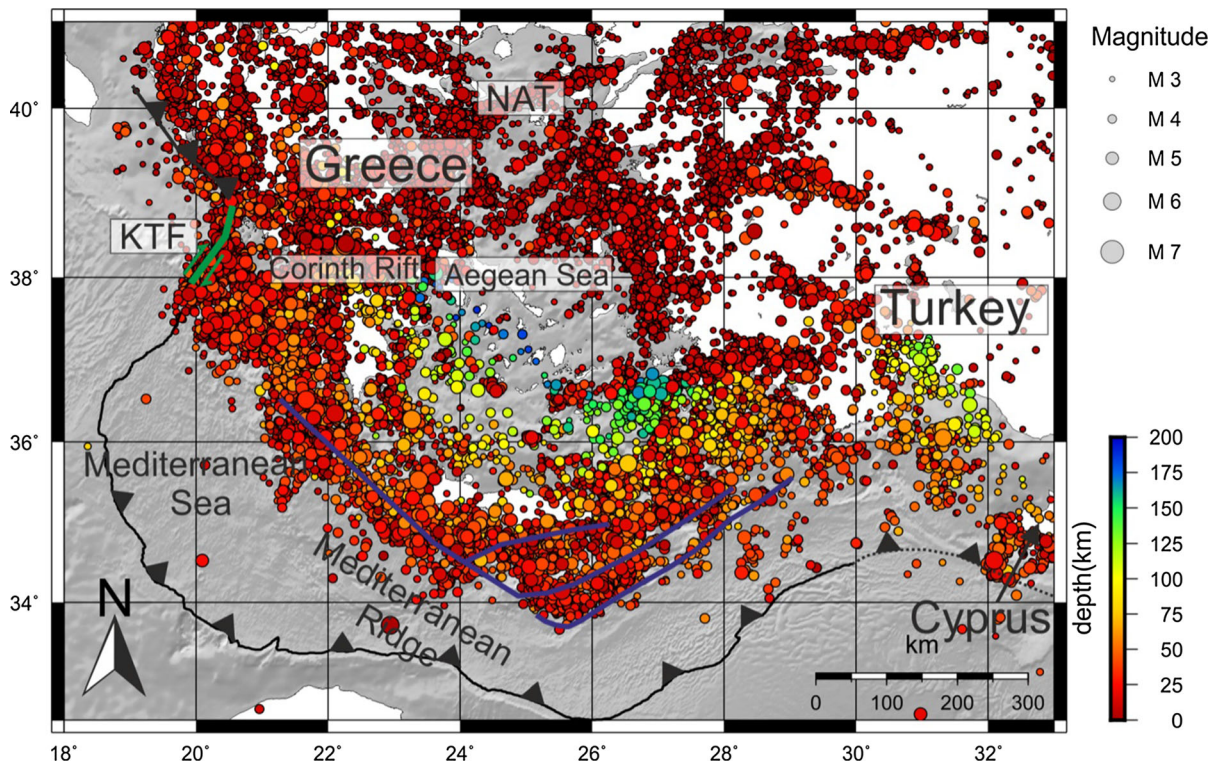
Figure 2
Distribution of instrumental seismicity at the Hellenic subduction zone for the period 1964–2016 (ISC 2017). Hypocentres are colour-coded according to depth and sized according to magnitude. Only earthquakes with horizontal and vertical errors smaller than 10 km are shown. *KTF* Kefalonia Transform Fault, *NAT* North Aegean Trough. Other tectonic elements are described in Fig. 1

different number of seismic stations used; (2) the type of phases used, namely at local, regional or teleseismic distances; and (3) the velocity models used. The NOA solution was obtained using phases recorded at stations from the Hellenic Unified Seismic Network (HUSN) only, while EMSC and ISC also included phases from stations at regional and teleseismic distances that allow the reduction of the azimuthal gap in the solution but do not necessarily lead to a better constrained hypocentre.

We collected and analysed the focal mechanisms published from several agencies to further understand the characteristics of the event (Fig. 3). Although they exhibit significant differences in terms of centroid coordinates, the fault plane solutions are quite similar, showing an almost pure reverse faulting for both nodal planes (Fig. 3). A minor strike-slip component is observed in few focal mechanism solutions (NOA and UPSL; see Fig. 3 for explanations). One of

the nodal planes dips to N-NNE (NE for AUTH) with an angle larger than 30° with the only exception being represented by the IPGP solution showing a lower-angle fault of 14° (Fig. 3). The other nodal plane dips S-SSW with an angle larger than 40°–50° (Fig. 3). Zahradnik et al. (2009) analysed the nodal planes of the earthquake combining them with the available hypocentral solutions soon after the earthquake and indicated the N-NNE-dipping nodal plane as the most likely one. The N-NNE-dipping nodal plane is consistent with the seismotectonic setting of the area and was also suggested by Shaw and Jackson (2010). The latter authors suggested that the July 1, 2009 earthquake occurred on a splay fault in the overriding plate whose projection on the sea bottom corresponds to a clear bathymetric scarp.

According to preliminary solutions aiming to define the causative fault plane (Zahradnik et al. 2009), previous literature about the event (Shaw and
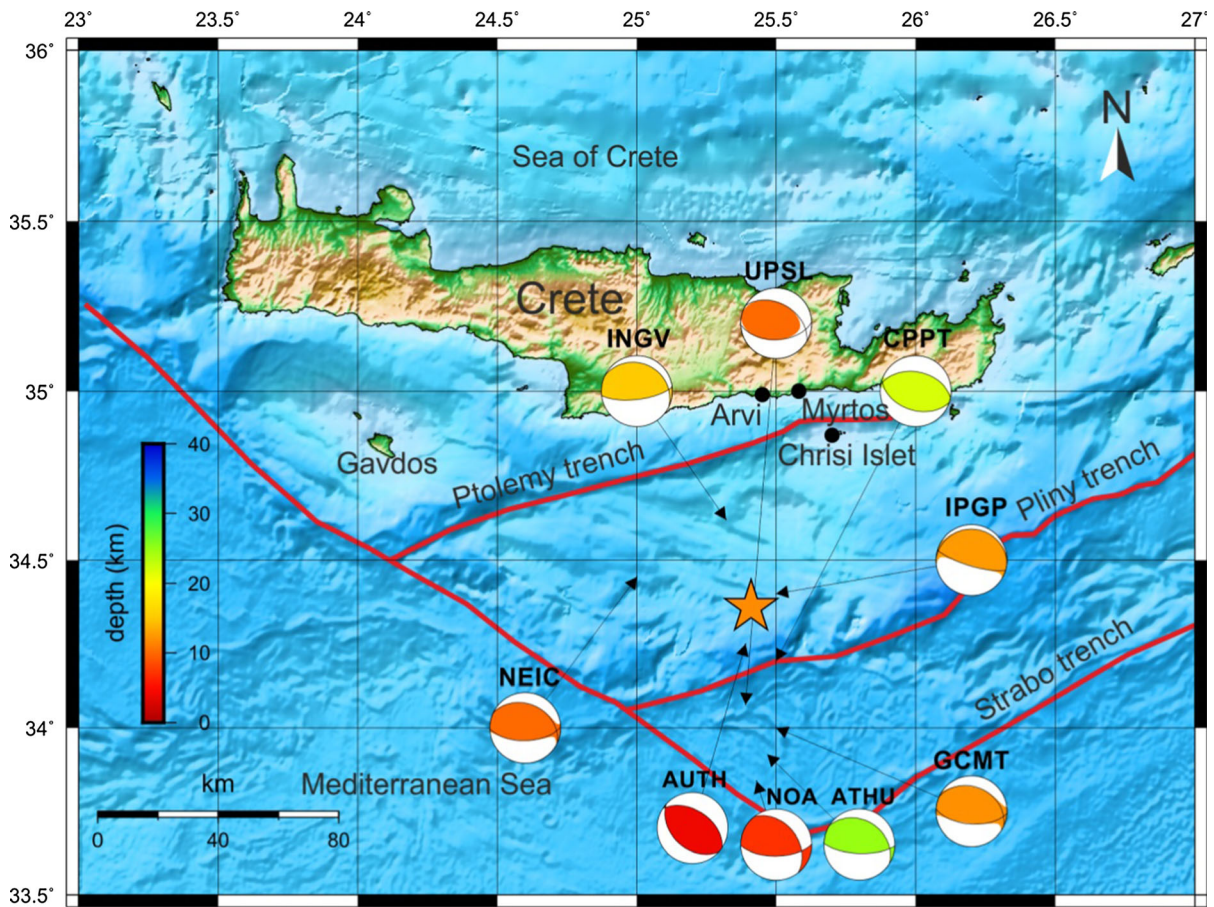
Figure 3

Focal mechanisms for the July 1, 2009 earthquake: *NEIC* National Earthquake Information Center, *INGV* Istituto Nazionale di Geofisica e Vulcanologia, *UPSL* University of Patra Seismic Laboratory, *CPPT* Centre Polynesien de Prevention des Tsunamis, *AUTH* Aristoteles University of Thessaloniki, *ATHU* University of Athens Seismic Laboratory, *NOA* National Observatory of Athens, *IPGP* Institut de Physique du Globe de Paris, *CMT* centroid moment tensors of Harvard. The focal mechanisms are coloured according to focal depth. The arrows starting from the beach balls point toward the epicentral coordinates of the earthquake's centroid obtained from the various agencies. The star indicates the epicentral location of the July 1, 2009 earthquake according to the relocation performed in this study using the 2-D velocity model. The three locations at which the tsunami was observed, namely Myrtos, Arvi, and Chrisi Islet, are indicated in the map

Jackson 2010), and the tectonic setting of the area (e.g., Taymaz et al. 1990; Shaw and Jackson 2010), the NNE-dipping nodal plane is assumed as the nodal plane of the event. Harvard's GCMT solution for M_w and for the focal parameters was preferred to other solutions mainly because it is the result of a world-wide-acknowledged methodology based on the inversion of teleseismic waveforms (Dziewonski et al. 1981; Ekström et al. 2012).

3.1. Earthquake Relocation

The July 1, 2009 south of Crete earthquake was relocated by using either: local 1-D velocity models (Delibasis et al. 1999; Meier et al. 2004; Becker et al. 2010; the velocity model used by NOA at the time of the earthquake; Fig. 1S); or a 2-D velocity model created to better resemble the crustal structure of the area (Fig. 2S). The 2-D velocity model was extracted from a refraction profile crossing the island of Crete from NNE–SSW (Bohnhoff et al. 2001). It extends from Antikythira to Karpathos in the x-direction and

from latitude of 33.85N to Santorini in the y-direction (Fig. 3S). The original refraction profile was properly adapted to the N–S direction and was extended a bit toward the north, by assuming a constant velocity structure, to include also the seismic station in Santorini (SANT) in the relocation. The original seismic refraction profile was also extended down to 60-km depth assuming a constant dipping angle of the slab and a constant velocity towards larger depths (Fig. 2S). We tried to include the highest possible number of stations to relocate the event taking into account regional crustal heterogeneities, especially in the E–W direction (Bohnhoff et al. 2001; Makris et al. 2013). N–S heterogeneities were in fact accounted by the constructed 2-D velocity model. Thus, we could not include stations farther than Karpathos to the east as well as farther than Antikythira to the west, or in the Peloponnese, because the constructed 2-D velocity model would not be valid. A constant V_p/V_s ratio of 1.78 was adopted according to the existing velocity models for the area (Meier et al. 2004).

To make all the hypocentral solutions relative to the different velocity models comparable, they were all calculated by using phase arrivals at the same seismic stations, the same weighting scheme, and the same software.

The local 1-D velocity models retrieved from the literature and used in the relocation (Fig. 1S) were obtained during microseismicity experiments employing mainly temporary land stations (Delibasis et al. 1999; Meier et al. 2004), and in some cases, also OBSs (Becker et al. 2010). We did not use station corrections provided by the original studies because of the different network configurations. The RMSs and the associated vertical and horizontal errors were calculated to rank the quality of the different solutions and select those to test in the tsunami simulations.

The relocations were performed by using the non-linear location (NLLoc) algorithm (Lomax et al. 2000). The non-linear location methods provide more reliable solutions and hypocentre error estimates than linearized location methods in case of ill-conditioned location problems as in this study (Lomax et al. 2009).

A total of ten stations (Fig. 3S) from the HUSN with 14 phases including P- and S-arrivals available from NOA were used to relocate the earthquake. In case of 1-D velocity models, the inclusion of stations at larger distances was observed to not improve the final solution and, therefore, they were not used. Karastathis et al. (2015) showed how the inclusion of phases at stations at distances larger than the critical distance lowers the quality of the hypocentral solutions when major structural heterogeneities in the velocity structure, as in the Hellenic forearc, are present.

The hypocentral solutions obtained from the relocation of the earthquake (Table 1) can be separated into two groups according to depth: (1) shallower hypocentres with depth shallower than 13 km are obtained by using 1-D velocity models having a Moho at about 30 km, and the 2-D velocity model built in this study; (2) deeper hypocentres of 28 and 40 km are obtained by using 1-D velocity models having a Moho at about 40 km (Table 1). These differences are to be expected because the earthquake

Table 1

Hypocentral solutions for the July 1, 2009 earthquake obtained by using different velocity models

Lat. (°)	Long. (°)	Depth (km)	Obs.	RMS (s)	H. err. (km)	V. err. (km)	Velocity model
34.36	25.41	11.7	14	0.2	2.8	2.9	2-D Bohnhoff et al. (2001)
34.39	25.40	12.1	14	0.27	3.9	3.8	1-D Meier et al. (2004)
34.38	25.38	12.6	14	0.23	3.0	3.6	1-D Delibases et al. (1999)
34.37	25.41	28	14	0.24	4.0	2.9	1-D NOA 2009
34.48	25.39	39.6	14	0.31	4.9	5.5	1-D Becker et al. (2010)

The locations and error estimates reported in the table have been obtained by using NLLoc

H. err. horizontal error, *V. err.* vertical error, *Obs.* number of observations

occurred about 80 km away from the closest station, where the head-wave (Pn) represents the first arrival. Thus, Moho depth differences in the velocity model have a first-order control on the hypocentral solution. The epicentral coordinates are observed to be less affected by the use of different velocity models (Table 1).

The 2-D velocity model provides the best results in terms of RMS and vertical and horizontal errors (Table 1). The maximum likelihood hypocentre and the posterior density function obtained by using the 2-D velocity model in NLLoc are reported in Fig. 4.

4. Modelling of the Local Tsunami

The July 1, 2009 south of Crete earthquake was followed by a small local tsunami which reportedly inundated the south-eastern coast of Crete and the northern coast of Chrisi Islet. To approach the best source model that produced the tsunami wave, we compared reported tsunami observations with synthetic tsunami features obtained through numerical simulations based on various homogeneous and heterogeneous slip models for the causative seismic fault.
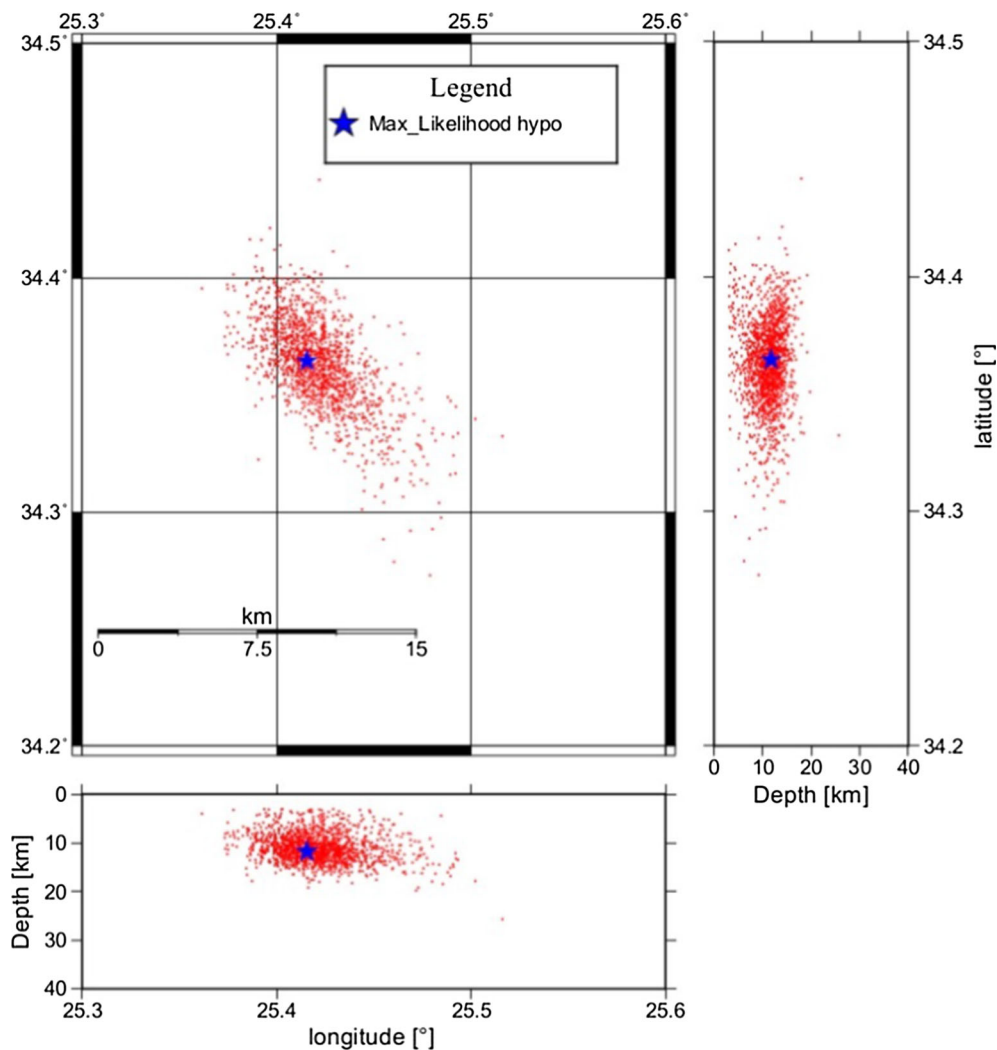

Figure 4
The maximum likelihood hypocentre (blue star) and the posterior density function (red cloud) of the July, 1 2009 south of Crete earthquake. The solution is obtained by using NLLoc, the 2-D velocity model and the seismic stations described in Fig. 3S

4.1. Tsunami Observations

The tsunami was not recorded at tide gauges, but it was observed by many eyewitnesses given its occurrence in summer, at 12.30 pm local time, when many people were on the beach. According to eyewitnesses accounts reported in local press, the tsunami was observed in the coastal localities of Myrtos and Arvi (south-eastern coast of Crete) and to the north of Chrisi Islet (Fig. 3). In Arvi, after a water retreat of about 1 m, four or five wave arrivals with amplitudes of up to 30 cm were reported. A video shoot recorded by an amateur and communicated to us shows the strong water withdrawal in Arvi. The sea disturbance lasted for about 1 h in Arvi and to the north of Chrisi Islet.

4.2. Homogeneous Fault Slip

The dimension of the causative seismic fault to use in the tsunami simulations with a homogeneous slip model was estimated by averaging the results from five empirical relationships all applicable to the analysed tectonic context. In fact, a direct estimation of the fault dimensions from the aftershocks distribution has not been possible due to the poor quality of aftershock determinations. We used empirical and semi-empirical relationships between the fault length (L) and width (W) and M_w or the seismic moment (M_0). We used M_0 obtained from the Harvard GCMT ($M_0 = 5.85 \times 10^{25}$ dyne cm) from which we calculated an M_w 6.45 applying the formula proposed by Hanks and Kanamori (1979):

$$M_w = 2/3 \times \mathrm{Log}_{10} M_0 - 10.73. \qquad (1)$$

These relationships included: (1) the well-known empirical relationship for reverse-fault earthquakes of Wells and Coppersmith (1994); (2) the empirical relationship for inter-plate earthquakes of Blaser et al. (2010); (3) the semi-empirical relationship for dip-slip earthquakes of Wang and Tao (2003); (4) the empirical relationship for dip-slip events of Leonard (2010); and (5) the empirical relationship for earthquakes in the Mediterranean Sea region of Konstantinou et al. (2005). The aforementioned empirical and semi-empirical relationships are reported in Table 1S. Concerning the fault length

(L), all the relationships give values ranging between 21 and 21.7 km, with the exception of the empirical relationship of Konstantinou et al. (2005) providing a length of 36 km. The obtained average value for the length is 24.2 km. The fault width (W) ranges from 11.1 to 13.5 km, with an average value of 12.3 km. Thus, the dimensions of our causative fault are 24.2×12.3 km leading to a rupture area $A = 298$ km^2. Applying the equation proposed by Hanks and Bakun (2002), relating the rupture area A with the M_w:

$$M_w = \mathrm{Log}A + 3.98(\pm 0.03), \qquad (2)$$

we obtain a M_w of 6.45 ± 0.03 supporting the estimated L and W values.

After the determination of the fault dimensions (L and W) we derived the average slip on the fault (D) by using the fundamental seismic moment equation introduced by Aki (1966):

$$M_0 = GDA. \qquad (3)$$

We obtained an average slip (D) of 65.5 cm using a rigidity modulus (G) of 30 GPa.

We placed the fault centroid at the epicentral coordinates estimated by relocating the July 1, 2009 earthquake with the 2-D velocity model and at varying depths according to the relocation results (Table 1). In particular, we used centroid depths of 25 km, 26 km, and 9.7 km to reproduce the scenario of an earthquake occurring: (1) along the inter-plate seismogenic zone, where the depth of the plate interface and its dipping angle beneath the calculated epicentral location were estimated from the micro-seismicity cross sections reported in Becker et al. (2010) and Bocchini et al. (2018); (2) at a hypocentral depth indicated in the revised NOA catalogue, similar to the hypocentral depth obtained herein using the same velocity model; (3) at a hypocentral depth obtained with the 2-D velocity model (Table 1). Centroid depths for scenarios 2 and 3 were estimated by assuming a unilateral up-dip propagation of the rupture from the hypocentre on a fault plane dipping 32°. The NNE-dipping nodal plane of the Harvard GCMT was used to define the strike 295°, dip 32°, and rake 108° of the causative fault.

We reproduced two additional scenarios involving the use of the heterogeneous and of the homogeneous

slip model on the same fault plane determined by the inversion of teleseismic data as described more in detail in Sect. 4.3.

4.3. Heterogeneous Fault Slip

To compute the spatial and temporal evolution of the slip on the causative fault, the kinematic, non-negative, least squares inversion technique by Hartzell and Heaton (1983) and Mendoza and Hartzell (2013) was applied. The finite-fault waveform inversion scheme developed by Hartzell and Heaton (1983) involves a trial-and-error procedure to obtain the best smoothing weight that identifies the simplest solution that still fits the data (Mendoza and Hartzell, 2013). The plot of residual norms $\|Kx - b\|$, where K is the sub-fault synthetics matrix, b is the matrix of observations, and x is the solution vector containing the slip required to reproduce the observations of the regularized solutions versus their corresponding smoothing norms $\|Lx\|$, forms an L-curve that quantifies the balance between fitting the data and meeting the smoothing constraints (Mendoza and Hartzell 2013). A rectangular fault plane, discretized into uniform cells (sub-faults) was constructed, and each point of the source response was computed with a code based on the generalized ray theory (Langston and Helmberger 1975). Synthetics were constructed following the discussion in the study of Heaton (1982). The calculated elementary synthetics were convolved with an attenuation operation under the assumption that $t^* = 1$ s, where t^* is the attenuation parameter of teleseismic body waves that represents the total body wave travel time divided by Q along the ray path for P waves (Stein and Wysession, 2003).

We used P-phases from 30 stations at teleseismic distances ranging from 30° to 90° with good azimuthal coverage (Fig. 4S). The waveform data were downloaded from the IRIS Data Management Centre (https://ds.iris.edu/ds/nodes/dmc/). All waveforms were pre-processed to remove the mean offset and instrument response before the inversion. They were also band-pass filtered between 0.03 and 0.09 Hz using a Butterworth filter, re-sampled to 0.2 samples/s and finally integrated in time to obtain displacements.

4.3.1 Fault Parameterization

Several values of source velocity, varying from 2.5 to 3.5 km/s, were examined. Rise time, fault dimensions, position and depth of the hypocentre, and time lag were also changed during the inversions. The source of the elementary synthetics was taken as a trapezoidal shape and the width of the source was chosen to be short enough, i.e., 0.5 s, compared to the total rise time on the fault using siz time windows. We performed the inversion to find the slip distribution assuming the NNE-dipping fault and a simple 1-D velocity model. The fault was discretised by 108 sub-faults, 18 of them along the strike and 6 along the dip. After several inversions, we ended up with a fault length of 27 km starting from the earth surface and going down to 12-km depth with a hypocentre at 9-km depth. Starting from the GCMT faulting parameters, it was found that the strike of the fault which gave us better solutions was 305° with a dip of 32°. During the inversion we left the rake to change from 70° to 130°.

The co-seismic slip distribution of the earthquake, representing the movement of the hanging wall with respect to the foot wall, is illustrated in Fig. 5. The time evolution of slip is presented in each case by six snaps using nearly 2.3-s intervals. The slip distribution is smoothed in 2-D, and a cone-shaped filter was applied.

The fitting between teleseismic waveforms and synthetics is shown in Fig. 5S. As observable from Fig. 5, the rupture started at 9 km depth and was strongly unilateral, showing a strong directivity towards the west with a velocity of 2.6 km/s. The rupture started with small values of slip (< 10 cm) and after about 4 s the slip moved upward and westward with larger values (up to more than 1 m). The M_0 calculated from the inversion $M_0 = 6 \times 10^{25}$ dyne cm is consistent with that determined by Harvard's GCMT solution. The earthquake's total rupture duration was shorter than 14 s. Maximum calculated co-seismic slip was 1.07 metres at about 13 km west from the hypocentre (Fig. 5).

The above described heterogeneous slip model was used to run tsunami numerical simulations (scenario 4, Table 2) in addition to the homogeneous models. We modelled an additional case, namely

Cross Section of Slip Distribution
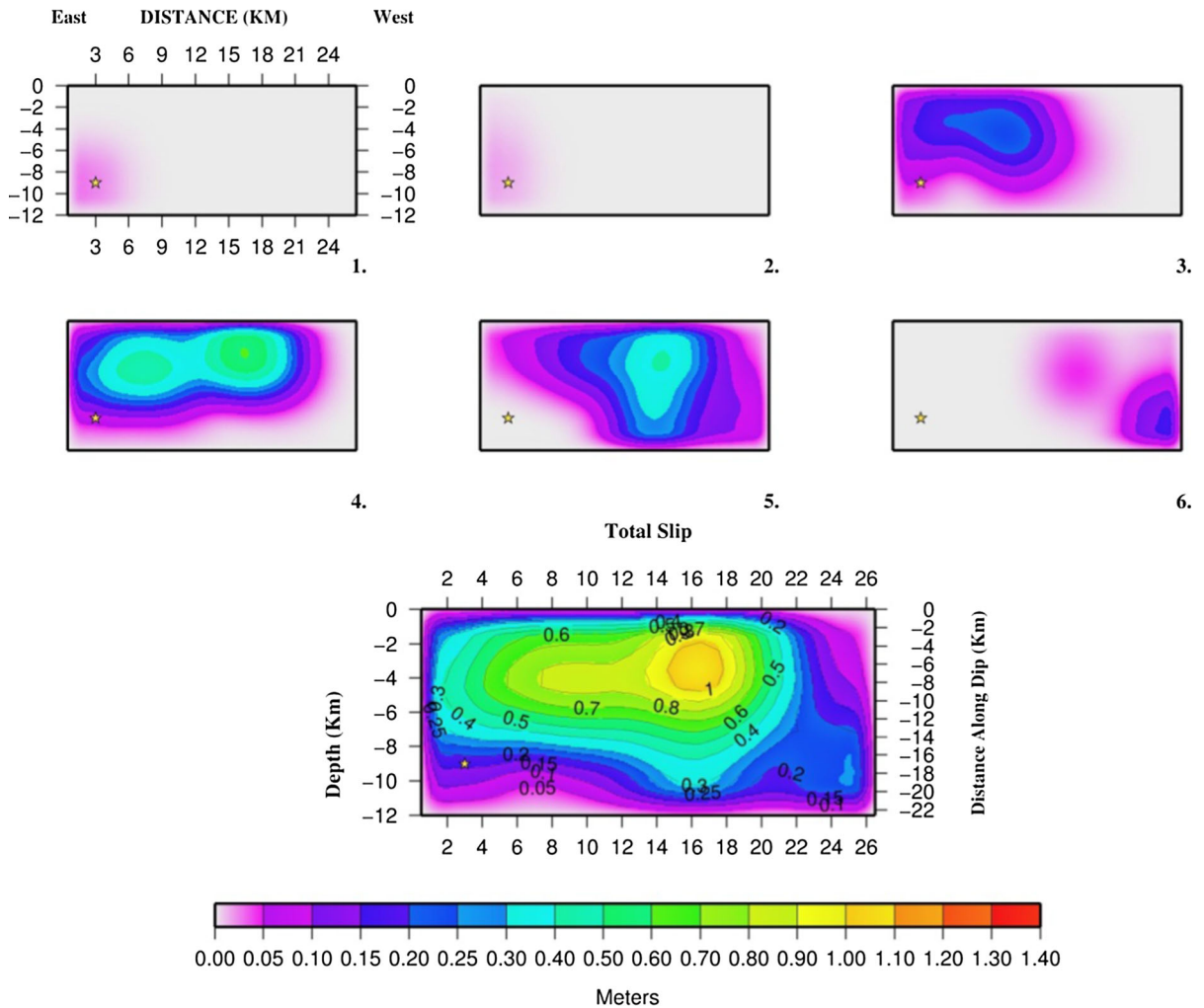
6 Snapshots of 2.30 Sec Duration

Figure 5
Cross section showing the temporal distribution of slip along the fault plate (1–6). The total slip on the fault is shown at the bottom part of the figure

scenario 5 (Table 2), to better compare the differences between homogeneous and heterogeneous slip models. In the latter case, we used the same fault parameters as for the heterogeneous fault model, but we averaged the slip above the fault plane.

4.4. Modelling of the Surface Deformation

The surface deformation due to a finite rectangular source on top of an elastic half-space was obtained through Okada (1985) modelling.

In particular, we employed a homogeneous (Sect. 4.2) and a heterogeneous fault slip model (Sect. 4.3) and further made a comparative analysis of the wave amplitudes calculated for the two cases. The cosesimic displacement produced by the heterogeneous slip model was obtained by applying the Okada's dislocation model (Okada 1985) to each of the sub-faults and summing up their contribution. A total amount of 108 sub-faults was used, 18 along strike and 6 along dip, with size of 1.5 × 3.6 km.

Table 2

Input parameters used for the tsunami simulations

	Scenario 1	Scenario 2	Scenario 3	Scenario 4	Scenario 5
Lat. (°)	34.4	34.4	34.4	34.4	34.4
Long. (°)	25.4	25.4	25.4	25.4	25.4
Centroid depth (km)	25[a]	26	7.7	[b]	6
Strike (°)	295	295	295	305	305
Dip (°)	15	32	32	32	32
Rake (°)	108	108	108	108	108
Average slip (m)	0.66	0.66	0.66	Heterogeneous	0.36
Length (km)	24.2	24.2	24.2	27	27
Width (km)	12.3	12.3	12.3	22	22
Shear modulus (GPa)	30	30	30		

[a]Depth of the plate interface beneath the earthquake epicentre

[b]The fault is discretised in sub-faults located at different centroid depths

The main geometrical and focal parameters describing the five scenarios resulting from the five different fault configurations, discussed in Sects. 4.2 and 4.3, are summarised in Table 2. The resulting deformation for all the modelled scenarios, representing the input for the tsunami modelling, is shown in Fig. 6. Maximum calculated vertical deformation was 5, 6, 25, 24, and 20 cm for scenario 1, 2, 3, 4, and 5, respectively.

The vertical component of the deformation obtained for the scenarios reproducing the case of an inter-plate earthquake (scenario 1, Table 2) and of the hypocentral solution obtained from NOA (scenario 2, Table 2), shows almost negligible deformation with a maximum vertical deformation of few cm (Fig. 6a, b), unable to explain the tsunamigenic nature of the earthquake. The aforementioned scenarios consider centroid depths of 25 km for the inter-plate earthquake (scenario 1) and of 26 km for NOA hypocentral solution (scenario 2). On the other hand, a maximum vertical deformation at surface of about 20–25 cm is observed for the scenarios employing a shallower centroid depth (scenarios 3–5, Fig. 6c–e). Thus, the shallower sources obtained by relocating the earthquake using the 2-D velocity model (scenario 3), and using the fault geometry constrained from the heterogeneous fault slip model (scenarios 4–5) produced vertical deformation at the surface compatible with the tsunamigenic nature of the earthquake.

4.5. Tsunami Modelling

Tsunami modelling was performed using the software package GEOWAVE (Watts et al. 2003), which is a combination of TOPICS (Tsunami Open and Progressive Initial Conditions System; Grilli and Watts 1999) and FUNWAVE (Wei and Kirby 1995; Wei et al. 1995). TOPICS uses a variety of curve fitting techniques to estimate the initial conditions, namely surface elevations and water velocities for tsunami propagation. FUNWAVE performs wave propagation simulation based on Boussinesq equations for the description of fully non-linear and dispersive waves, allowing the estimation of accurate run-ups and inundation at the same time. FUNWAVE includes also well-calibrated dissipation models for wave breaking and bottom friction. For the present study, however, we noticed that Boussinesq and non-linear shallow water (NLSW) models show similar results (Fig. 6S).

Time histories of the tsunami waves were calculated at synthetic tide gauges placed close to the locations where the tsunami was observed, namely: (1) Arvi; (2) Myrtos; and (3, 4) to the North of the Chrisi Islet (Fig. 7a). Unfortunately, as already mentioned, no operating tide gauges were in place at the time of the earthquake in the areas hit by the tsunami. Thus, a direct comparison between observed and calculated tsunami wave amplitudes at tide gauges was not possible. Therefore, we calculated time histories of tsunami waves in proximity of the sites where the tsunami was observed (Fig. 7a) with
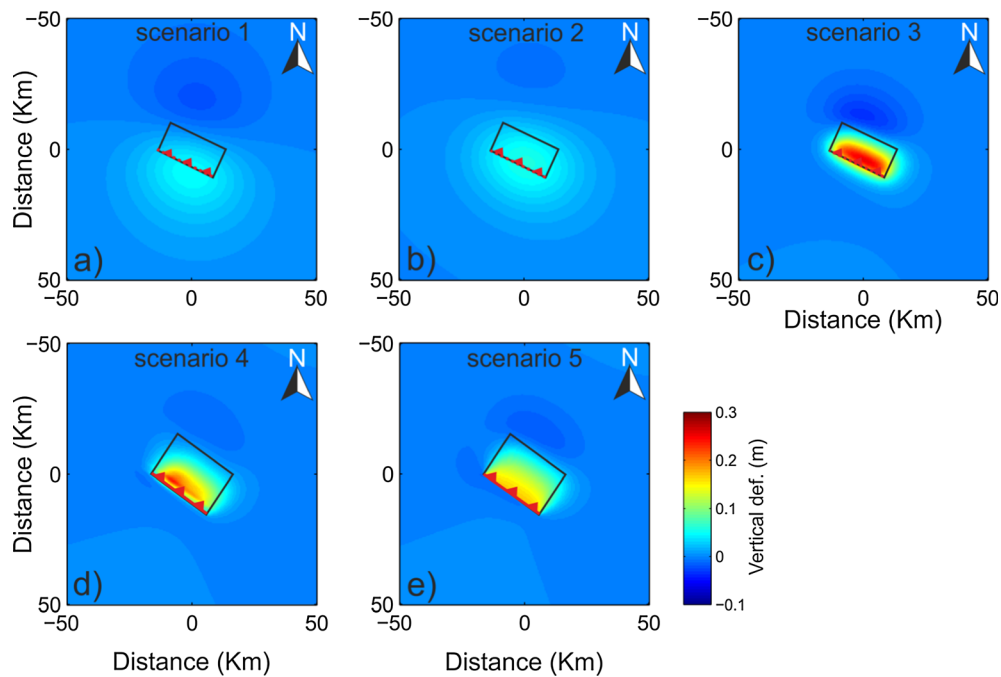
Figure 6
Vertical component of the deformation vector calculated for the faults with characteristics summarised in Table 3. The surface deformation is obtained by using the analytical solution of Okada (1985). The black rectangles within the subplot indicate the surface projection of the fault modelled in each scenario. The red lines indicate location of the up-dip limit of the fault while the barbs the dipping direction of the fault. In case of scenarios 1, 2 and 3 the red lines is dotted because by construction the fault did not reach to the sea bottom as in the case of scenarios 4 and 5. The centre of the plot (0, 0) coincides with the fault centroid

the aim to compare results from tsunami simulations with eyewitnesses' observations. The time step used for the tsunami simulations was of 0.1243 s.

The reference grid to model tsunami propagation in the sea was constructed by using the bathymetry grid from the European Marine Observation and Data Network (EMODnet) project (EMODnet DTM version released in 2018, http://www.emodnet.eu/), which has a resolution of about 115 m. Since the EMODnet bathymetry does not resolve areas above the sea level (a standard positive number is assigned to all the areas lying above the sea level), we used the topography grid from the Shuttle Radar Topography Mission with a resolution of 30 m (SRTM30; https://dwtkns.com/srtm30m/) to better resolve areas above the sea level and to account for possible interactions of the tsunami waves with the shoreline. The SRTM30 topography grid was resized and merged with the EMODnet bathymetry grid by using the Global Mapper tool v. 13. Both grids were freely

available online. The final grid employed for tsunami wave modelling is shown in Fig. 7a. The coastline geometry employed in tsunami modelling (Fig. 7a) shows good agreement with the coastline observed in Google Earth for the same region (Fig. 7b).

The mareograms calculated at the synthetic tide gauges (Fig. 7a) are shown in Fig. 8. A synthesis of the results with the absolute maximum amplitudes calculated at each tide gauge for the five scenarios are reported in Table 3.

The implementation of a low-resolution bathymetry grid, i.e., ~ 115 m, prevents a direct comparison between calculated and observed tsunami wave amplitudes at the shore. In fact, although we use the best bathymetry source available to us, possible amplification or attenuation phenomena associated to tsunami waves at the shoreline are not well reproduced because of the low bathymetry resolution (an amplification factor of 2–5 on wave heights could locally occur). Thus, we limit the
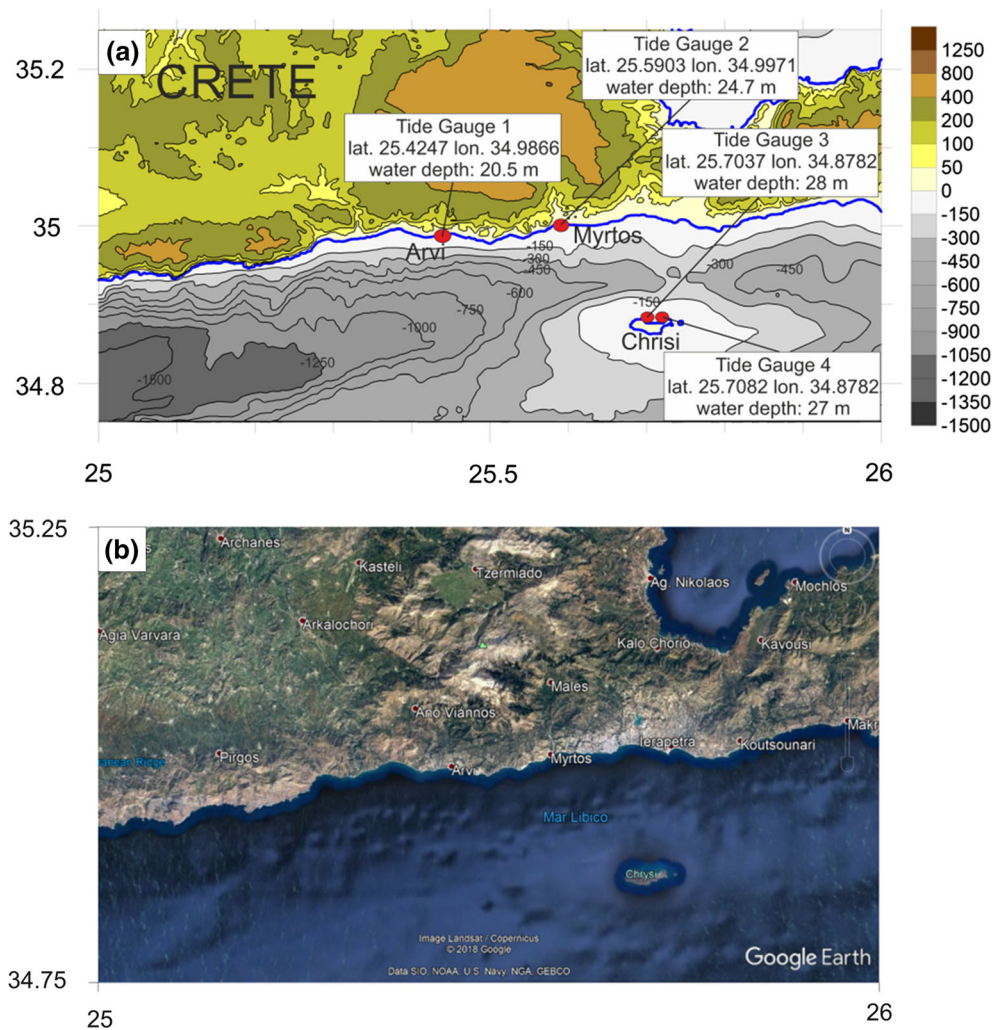
Figure 7
a Plot of the grid file and of the tide gauges used for tsunami modelling. Water depth and coordinates of the synthetic tide gauges are reported. The bathymetry is taken from EMODNet DTM 2018 while the topography from the SRTM (see text for the description of the grid files). **b** Google map screen shot of the region shown in sub-figure a

description of the results to the general trends of calculated mareograms. Tide gauges are located at similar water depths, between 20.5 and 28 m (Fig. 7a), for a relative comparison of the synthetic mareograms. We could not place tide gauges at shallower water depths because results would become more instable.

From the synthetic mareograms in Fig. 8 it is possible to distinguish two sets of solutions: (1) those showing longer-period waves with lower amplitudes (scenarios 1–2); and (2) those showing shorter-period waves with larger amplitudes (scenarios 3–5). The first set of solutions (red and black lines, Fig. 8), showing low-amplitude waves, are obtained by using deeper centroid depths (25 km for scenario 1 and 26 km for scenario 2) and homogeneous slip on the causative fault (see Table 2 for input parameters). In addition, calculated wave amplitudes for scenarios 1 and 2 do not show significant variations at the different tide gauges as instead observed for the other three scenarios (scenarios 3–5, Fig. 8; Table 3). The Okada analytical solution for displacement provides
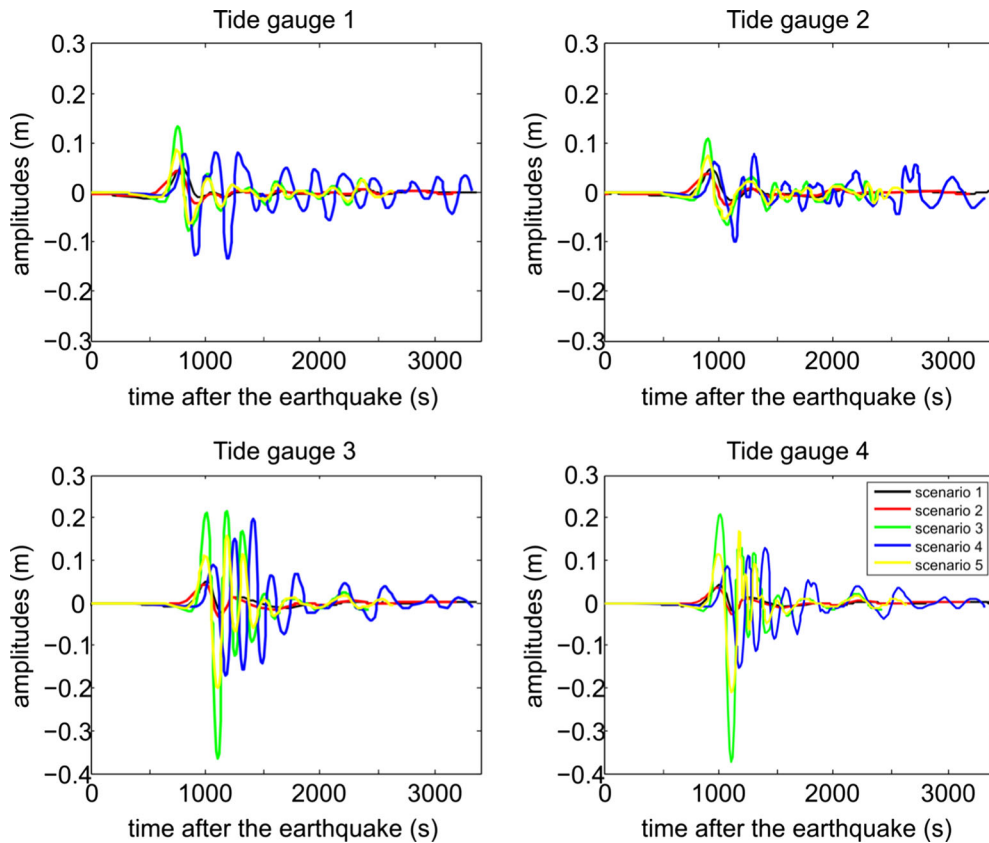
Figure 8
Mareograms calculated for the five different scenarios detailed in Table 2 at the synthetic tide gauges shown in Fig. 7a. Maximum and minimum synthetic tsunami waves are reported in Table 3

negligible vertical deformation associated with the aforementioned scenarios (scenarios 1–2, Fig. 6).

The other set of solutions, showing larger-amplitude waves were obtained by using shallower centroid depths (6 or 7.7 km) and both homogeneous and heterogeneous slip on the causative fault (scenarios 3–5, see Table 2 for input parameters). A clear oscillation in the signal indicates the passage of the tsunami waves starts about 500–600 s after the earthquake origin time (Fig. 8). The largest tsunami wave amplitudes are calculated at synthetic tide gauges located to the north of Chrisi Islet (scenarios 3–5, Fig. 8; Table 3). We can neither confirm nor exclude such result because we do not have official reports of tsunami waves observed at the northern shoreline of Chrisi Islet. We speculate that a possible explanation for the larger wave amplitudes calculated to the north of Chrisi Islet, with respect to those close

to the sites of Arvi and Myrtos (Fig. 7a, Table 3), could be due to the fact that the wave was trapped to the north of the Islet, because of the morphology of the shoreline (Fig. 9), and amplified by multiple reflection.

Scenario 3, namely the one calculated for a fault having a centroid depth of 7.7 km and homogeneous slip, generates the largest wave amplitudes (Table 3). Scenarios 4 and 5, namely the scenario reproducing heterogeneous slip on the causative fault and the scenario reproducing homogenous slip on the same fault (Table 2), generate similar zero-to-peak amplitudes at tide gauges located close to Arvi and Myrtos. Larger zero-to-trough amplitudes at the same tide gauges are observed for scenario 4 (Table 3). At tide gauges located to the north of Chrisi Island (tide gauges 3 and 4; Fig. 7a), scenario 5 produces zero-to-trough amplitudes larger than those observed for

Table 3

Zero-to-peak (+) and zero-to-trough (−) tsunami wave amplitudes (m) at the synthetic tide gauges shown in Fig. 7. Values are taken from Fig. 8

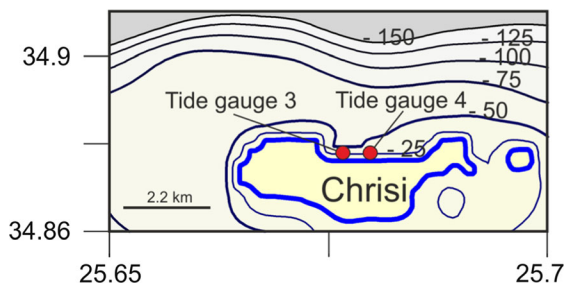| Tide gauge #	Synthetic tsunami wave amplitudes (m)									
	Scenario 1		Scenario 2		Scenario 3		Scenario 4		Scenario 5	
	+	−	+	−	+	−	+	−	+	−
Tide gauge 1	0.05	0.01	0.04	0.02	0.134	0.077	0.082	0.134	0.087	0.064
Tide gauge 2	0.05	0.01	0.04	0.02	0.108	0.065	0.076	0.098	0.073	0.054
Tide gauge 3	0.05	0.02	0.04	0.03	0.215	0.365	0.199	0.175	0.16	0.2
Tide gauge 4	0.04	0.02	0.03	0.03	0.21	0.37	0.13	0.153	0.17	0.21

Figure 9
Closer view of Chrisi Islet and surrounding bathymetry. Red circles indicate the location of synthetic tide gauges. The thick blue line defines the shoreline

scenario 4 (Table 3), while zero-to-peak amplitudes are larger for scenario 5 at one tide gauge (tide gauge 4, Table 3) and for scenario 4 at the other tide gauge (tide gauge 3, Table 3). The scenario reproducing the heterogeneous slip on the fault, namely scenario 4, shows synthetic tsunami wave oscillations lasting longer with respect to the other scenarios (Fig. 8). In fact, after about 1200–1500 s, synthetic waves calculated for scenarios 1 and 2 are not visible anymore, while they are still visible but with very small amplitudes for scenarios 3 and 5. According to eyewitnesses, the sea disturbance lasted about 1 h in Arvi and to the north of Chrisi Islet. Thus, the scenario involving the heterogeneous slip model on the fault seems to better reproduce the observed sea disturbance among all considered scenarios. The same is also valid for the number of tsunami waves reaching the south-eastern coast of Crete. Eyewitnesses reported four or five tsunami waves in Arvi. At the synthetic tide gauge close to Arvi, at least three significant waves are observed for scenario 4 (tide gauge 1, Fig. 8). Instead, at the same tide gauge, for

scenarios 3 and 5, a first arrival with quite large amplitude is observable, and it is followed by only one other clear wave, however, of much smaller amplitude (tide gauge 1, Fig. 8).

Interestingly enough, for all the modelled scenarios, the tsunami wave oscillations calculated at the several synthetic tide gauges start with negative amplitude (Fig. 8), which implies water retreat. This negative amplitude, although very small, is consistent with the water withdrawal described by eyewitness before the first tsunami wave arrival in Arvi and verified by a video recorded soon after the earthquake occurrence.

5. Discussion: Implications on Tsunami Hazard Assessment and Early Warning

Results from the relocation of the July 1, 2009 earthquake and its tsunamigenic nature indicate a shallow depth of the seismic source. The modelling of both the surface deformation according to Okada's approach (Okada 1985) and of the tsunami waves allow exclusion of the deep source (scenario 2) and the inter-plate nature of the event (scenario 1). An upper-plate origin of the event, as already proposed by Shaw and Jackson (2010), is favoured. The upper-plate origin of the event is also supported by: (1) the calculated hypocentral depth of 11.7 km, that is shallower than the depth of the plate interface beneath its epicentral location, as indicated by microseismicity studies (Becker et al. 2010; Bocchini et al. 2018); (2) the event focal mechanism solutions (Fig. 3) exhibiting for the most likely nodal plane, namely the one dipping towards either N or NNE, a

reverse fault with a dip angle larger than 30°. The fault dip angle suggested by most of the focal mechanisms is observed to be steeper than the dip angle of the plate interface in the area ($\sim 15°$) inferred by the distribution of microseismicity (Becker et al. 2010; Bocchini et al. 2018).

The 2-D velocity model provides a better constraint of the hypocentral solution. Smaller vertical and horizontal errors as well as RMS with respect to the 1-D velocity models are observed. This underlies the importance of accounting for crustal thickness variations in the overriding plate when the sources to be located are situated, with respect to the receivers, at distances larger than the critical distance (e.g., Karastathis et al. 2015). However, the final hypocentre obtained relocating the event with some of the 1-D velocity models (i.e., Delibasis et al. 1999; Meier et al. 2004) is comparable with the hypocentre obtained using the 2-D velocity model. This is likely due to the configuration of the stations used in the inversion, which are located in regions with crustal thickness and velocity structure compatible with the aforementioned 1-D velocity models.

Scenario 4 reproducing the heterogeneous slip fault model, as well as scenarios 3 and 5 reproducing shallow centroid depths and homogeneous slip on the fault, are able to generate tsunami waves. Although we observe clear differences in the synthetic mareograms, especially between the scenarios involving homogeneous slip on fault and the one involving heterogeneous slip, we are unable to conclude which of them reproduces better the observations. A finer bathymetry grid, with resolution of about 20 m, would be needed to model tsunami waves at shore and perform a direct comparison with the maximum observed tsunami heights (~ 30 cm in Arvi). According to the general trends of synthetic mareograms, scenario 4 seems to better reproduce the observations with respect to scenarios 3 and 5 in terms of duration of the sea disturbance and number of observed tsunami waves. In fact, the scenario reproducing the heterogeneous slip on fault shows a longer disturbance of the sea and a larger number of tsunami waves.

Due to various sources of uncertainties, it is hard to draw deeper conclusions between observed and estimated tsunami wave amplitudes. Sources of uncertainty include the absence of tide gauge records, the low resolution of the bathymetry grid, and the characterization of the causative fault. Furthermore, uncertainties involved in eyewitness observations are also to be taken into account.

The results suggest that for moderate-magnitude earthquakes, as in the case of the July 1, 2009 earthquake M_w 6.45, the tsunami modelling performed by using the homogeneous slip model on the fault is comparable with the heterogeneous one in terms of maximum tsunami wave amplitudes if the fault parameters are carefully estimated. However, in terms of sea disturbance and number of tsunami waves, the model reproducing heterogeneous slip on the fault seems to better reproduce the observations. This is often the case of large earthquakes where the models considering heterogeneous slip on faults are capable to better reproducing the tsunami observations (e.g., Geist and Dmowska 1999).

This study highlights the tsunamigenic potential of upper-plate faults as observed also for recent tsunamigenic earthquakes in the Aegean (Heidarzadeh et al., 2017; Yalciner et al., 2017; Papadimitriou et al., 2018). In fact, it shows how even moderate-magnitude ($M_w < 6.5$), shallow earthquakes (depth < 12 km) rupturing relatively steep reverse faults (dip $> 30°$) can trigger tsunamis. Upper-plate reverse faults in the HSZ have been suggested to coincide with pronounced bathymetric features on the ocean floor (Shaw et al. 2008; Mouslopoulou et al. 2015), indicating their facility to displace the sea bottom and, therefore, their high tsunamigenic potential. Due to the shallower centroid depths and the steeper dip angles, the tsunamigenic potential of upper-plate reverse faults in the outer forearc is expected to be higher than that of inter-plate earthquakes of similar magnitude. Given the steeper dip angle, splay faults above the plate interface tend to produce a sharper vertical deformation which is more prone to generate a tsunami with respect to inter-plate earthquakes of similar magnitude (e.g., Wendt et al. 2009). In fact, possible inter-plate earthquakes with magnitude as large as 6.5 (1972-05-04) or even 7.0 (1952-12-17) have occurred south of Crete and have not triggered tsunamis (Papadopoulos 2011). Also, no tsunami observations were reported for the M_w 6.85 February 14, 2008

earthquake in southwestern Peloponnese, the strongest instrumentally well-recorded inter-plate earthquake in Greece (e.g., Howell et al. 2017). A very tiny tsunami wave of 3 cm (6 cm peak to trough) was recorded at the tide gauge in Kasteli (Crete) in the aftermath of the M_w 6.76 inter-plate earthquake (Howell et al. 2017) occurred west of Crete on October 12, 2013 (Dr. Charalampakis M. pers. comm., NOA). Despite the larger magnitude with respect to the July 1, 2009, the October 12, 2013 earthquake generated a much smaller tsunami because of the larger depth ($\sim$ 45 km) and of the lower dip angle ($\sim$ 12°) of the causative fault.

Tsunami simulations show the very short time ($\sim$ 10 min) needed by the first tsunami waves to reach the southern coast of Crete, posing a big challenge for early warning systems. These small tsunamigenic earthquakes are quite challenging to test and calibrate capabilities of tsunami early warning systems. Currently, the Hellenic National Tsunami Warning Center (http://hl-ntwc.gein.noa.gr/) and other tsunami service providers operating in the North East Atlantic and Mediterranean Tsunami Warning System under the coordination of IOC/UNESCO have recommended 10 min as the target time for the release of the first tsunami message. A posteriori scenarios of early warning can be reproduced to understand drawbacks and strengths of the operational early warning systems.

6. Conclusions

The M_w 6.45 July 1, 2009 tsunamigenic earthquake ruptured the overriding plate to the south of Crete as indicated by the fault dipping angle retrieved by focal mechanism solutions, the relocated hypocentre calculated with a 2-D velocity model, and by the modelling of the small ensuing tsunami.

The use of a 2-D velocity model provides a slightly better constrain on the solution as compared to the 1-D velocity models since it accounts for the strong crustal thickness variations existing in the N–S direction across Crete, from the plate boundary towards the back-arc region.

The comparison of synthetic tsunami waves with eyewitness observations suggests that for earthquakes with magnitudes similar to the July 1, 2009 event, the heterogeneous slip model on the causative fault generates better results than the homogeneous slip model in terms of number of tsunami waves reaching the coast and of duration of the sea disturbance. However, although we observe different maximum amplitudes between scenarios involving heterogeneous and homogeneous slip on the causative fault, we cannot conclude which of them fits better with the observed tsunami heights.

This study highlights the high tsunamigenic potential associated with high-angle reverse faults in the upper-plate above the plate interface, higher than that of inter-plate earthquakes of similar or even slightly larger moment magnitude.

Tsunami simulations show the very short time, about 10 min, needed by the first tsunami waves to hit the southern coast of Crete, posing a big challenge for tsunami early warning systems.

Acknowledgements

Publisher's Note   Springer Nature remains neutral with regard to jurisdictional claims in published maps and institutional affiliations.

REFERENCES

Aki, K. (1966). Generation and propagation of G waves from the Niigata Earthquake of June 16, 1964. Part 2. Estimation of

earthquake movement, released energy, and stress–strain drop from the G wave spectrum. *Bulletin. Earthquake Research Institute, University of Tokyo, 44,* 73–88.

Ambraseys, N. (2009). *Earthquakes in the Mediterranean and Middle East: A multidisciplinary study of seismicity up to 1900.* Cambridge: Cambridge University Press. https://doi.org/10.1017/CBO9781139195430.

Becker, D., Meier, T., Bohnhoff, M., & Harjes, H.-P. (2010). Seismicity at the convergent plate boundary offshore Crete, Greece, observed by an amphibian network. *Journal of Seismology, 14,* 369–392. https://doi.org/10.1007/s10950-009-9170-2.

Blaser, L., Krüger, F., Ohrnberger, M., & Scherbaum, F. (2010). Scaling relations of earthquake source parameter estimates with special focus on subduction environment. *Bulletin of the Seismological Society of America, 100,* 2914–2926.

Bocchini, G. M., Brüstle, A., Becker, D., Meier, T., van Keken, P. E., Ruscic, M., et al. (2018). Tearing, segmentation, and back-stepping of subduction in the Aegean: New insights from seismicity. *Tectonophysics, 734–735,* 96–118. https://doi.org/10.1016/j.tecto.2018.04.002.

Bohnhoff, M., Makris, J., Papanikolaou, D., & Stavrakakis, G. (2001). Crustal investigation of the Hellenic subduction zone using wide aperture seismic data. *Tectonophysics, 343,* 239–262. https://doi.org/10.1016/S0040-1951(01)00264-5.

Delibasis, N., Ziazia, M., Voulgaris, N., Papadopoulos, T., Stavrakakis, G., Papanastassiou, D., et al. (1999). Microseismic activity and seismotectonics of Heraklion area (central Crete Island, Greece). *Tectonophysics, 308,* 237–248. https://doi.org/10.1016/S0040-1951(99)00076-1.

Dziewonski, A. M., Chou, T., & Woodhouse, J. H. (1981). Determination of earthquake source parameters from waveform data for studies of global and regional seismicity. *Journal of Geophysical Research: Earth, 86,* 2825–2852.

Ekström, G., Nettles, M., & Dziewoński, A. M. (2012). The global CMT project 2004–2010: Centroid-moment tensors for 13,017 earthquakes. *Physics of the Earth and Planetary Interiors, 200,* 1–9.

Galanopoulos, A. G. (1957). The seismic sea wave of July 9, 1956. *Prakt Academy Athens, 32,* 90–101.

Geist, E. L., & Dmowska, R. (1999). Local tsunamis and distributed slip at the source. *Pure and Applied Geophysics, 154,* 485–512. https://doi.org/10.1007/s000240050241.

Grilli, S. T., & Watts, P. (1999). Modeling of waves generated by a moving submerged body. Applications to underwater landslides. *Engineering Analysis with Boundary Elements, 23,* 645–656.

Guidoboni, E., & Comastri, A. (1997). The large earthquake of 8 August 1303 in Crete: Seismic scenario and tsunami in the Mediterranean area. *Journal of Seismology, 1,* 55–72. https://doi.org/10.1023/A:1009737632542.

Guidoboni, E., & Comastri, A. (2005). *Catalogue of earthquakes and tsunamis in the Mediterranean area from the 11th to the 15th century.* Rome: Istituto nazionale di geofisica e vulcanologia.

Hanks, T. C., & Bakun, W. H. (2002). A bilinear source-scaling model for M-log A observations of continental earthquakes. *Bulletin of the Seismological Society of America, 92,* 1841–1846. https://doi.org/10.1785/0120010148.

Hanks, T. C., & Kanamori, H. (1979). A moment magnitude scale. *Journal of Geophysical Research: Solid Earth, 84,* 2348–2350.

Hartzell, S. H., & Heaton, T. H. (1983). Inversion of strong ground motion and teleseismic waveform data for the fault rupture history of the 1979 Imperial Valley, California, earthquake. *Bulletin of the Seismological Society of America, 73,* 1553–1583.

Heaton, T. H. (1982). The 1971 San Fernando earthquake: A double event? *Bulletin of the Seismological Society of America, 72,* 2037–2062.

Heidarzadeh, M., Necmioglu, O., Ishibe, T., & Yalciner, A. C. (2017). Bodrum-Kos (Turkey–Greece) Mw 6.6 earthquake and tsunami of 20 July 2017: A test for the Mediterranean tsunami warning system. *Geoscience Letters.* https://doi.org/10.1186/s40562-017-0097-0.

Howell, A., Jackson, J., Copley, A., McKenzie, D., & Nissen, E. (2017). Subduction and vertical coastal motions in the eastern Mediterranean. *Geophysical Journal International, 211*(1), 593–620. https://doi.org/10.1093/gji/ggx307.

ISC, 2017. Reviewed International Seismological Centre (ISC) Bulletin. http://www.isc.ac.uk. Accessed 7 Jan 17.

Karastathis, V. K., Mouzakiotis, E., Ganas, A., & Papadopoulos, G. A. (2015). High-precision relocation of seismic sequences above a dipping Moho: The case of the January–February 2014 seismic sequence on Cephalonia island (Greece). *Solid Earth, 6,* 173.

Kiratzi, A., & Louvari, E. (2003). Focal mechanisms of shallow earthquakes in the Aegean Sea and the surrounding lands determined by waveform modelling: A new database. *Journal of Geodynamics, 36,* 251–274. https://doi.org/10.1016/S0264-3707(03)00050-4.

Konstantinou, K. I., Papadopoulos, G. A., Fokaefs, A., & Orphanogiannaki, K. (2005). Empirical relationships between aftershock area dimensions and magnitude for earthquakes in the Mediterranean Sea region. *Tectonophysics, 403,* 95–115.

Koulakov, I., & Sobolev, S. V. (2006). Moho depth and three-dimensional P and S structure of the crust and uppermost mantle in the Eastern Mediterranean and Middle East derived from tomographic inversion of local ISC data. *Geophysical Journal International, 164,* 218–235.

Langston, C. A., & Helmberger, D. V. (1975). A procedure for modelling shallow dislocation sources. *Geophysical Journal International, 42,* 117–130.

Leonard, M. (2010). Earthquake fault scaling: Self-consistent relating of rupture length, width, average displacement, and moment release. *Bulletin of the Seismological Society of America, 100,* 1971–1988.

Li, X., Bock, G., Vafidis, A., Kind, R., Harjes, H. P., Hanka, W., et al. (2003). Receiver function study of the Hellenic subduction zone: Imaging crustal thickness variations and the oceanic Moho of the descending African lithosphere. *Geophysical Journal International, 155,* 733–748. https://doi.org/10.1046/j.1365-246X.2003.02100.x.

Lomax, A., Michelini, A., & Curtis, A. (2009). Earthquake location, direct, global-search methods. In R. A. Meyers (Ed.), *Encyclopedia of complexity and systems science* (pp. 2449–2473). New York: Springer. https://doi.org/10.1007/978-0-387-30440-3_150.

Lomax, A., Virieux, J., Volant, P., & Berge-Thierry, C. (2000). Probabilistic earthquake location in 3D and layered models. In C. H. Thurber & N. Rabinowitz (Eds.), *Advances in seismic event location* (pp. 101–134). Dordrecht: Springer. https://doi.org/10.1007/978-94-015-9536-0_5.

Makris, J., Papoulia, J., & Yegorova, T. (2013). A 3-D density model of Greece constrained by gravity and seismic data. *Geophysical Journal International, 194,* 1–17.

McClusky, S., Balassanian, S., Barka, A., Demir, C., Ergintav, S., Georgiev, I., et al. (2000). Global positioning system constraints on plate kinematics and dynamics in the eastern Mediterranean and Caucasus. *Journal of Geophysical Research: Solid Earth, 105,* 5695–5719. https://doi.org/10.1029/1999JB900351.

Meier, T., Rische, M., Endrun, B., Vafidis, A., & Harjes, H.-P. (2004). Seismicity of the Hellenic subduction zone in the area of western and central Crete observed by temporary local seismic networks. *Tectonophysics, 383,* 149–169. https://doi.org/10.1016/j.tecto.2004.02.004.

Mendoza, C., & Hartzell, S. (2013). Finite-fault source inversion using teleseismic P waves: Simple parameterization and rapid analysis. *Bulletin of the Seismological Society of America, 103,* 834–844.

Mouslopoulou, V., Nicol, A., Begg, J., Oncken, O., & Moreno, M. (2015). Clusters of megaearthquakes on upper plate faults control the Eastern Mediterranean hazard. *Geophysical Research Letters, 42,* 10282–10289. https://doi.org/10.1002/2015GL066371.

Okada, Y. (1985). Surface deformation due to shear and tensile faults in a half-space. *Bulletin of the Seismological Society of America, 75,* 1135–1154.

Papadimitriou, P., Kassaras, I., Kaviris, G., Tselentis, G. A., Voulgaris, N., Lekkas, E., et al. (2018). The 12th June 2017 Mw = 6.3 Lesvos earthquake from detailed seismological observations. *Journal of Geodynamics, 115,* 23–42. https://doi.org/10.1016/j.jog.2018.01.009.

Papadopoulos, G. A. (2011). *A seismic history of Crete: Earthquakes and tsunamis, 2000 B.C.–A.D. 2010.* Athens: Ocelotos Publications.

Papadopoulos, G. A., Gràcia, E., Urgeles, R., Sallares, V., De Martini, P. M., Pantosti, D., et al. (2014). Historical and prehistorical tsunamis in the Mediterranean and its connected seas: Geological signatures, generation mechanisms and coastal impacts. *Marine Geology, 354,* 81–109. https://doi.org/10.1016/J.MARGEO.2014.04.014.

Papazachos, B. C., & Papazachou, C. (2003). *The earthquakes of Greece.* Thessaloniki: Ziti Publications. **(in Greek)**.

Reilinger, R., McClusky, S., Vernant, P., Lawrence, S., Ergintav, S., Cakmak, R., et al. (2006). GPS constraints on continental deformation in the Africa–Arabia–Eurasia continental collision zone and implications for the dynamics of plate interactions. *Journal of Geophysical Research: Solid Earth.* https://doi.org/10.1029/2005JB004051.

Sachpazi, M., Laigle, M., Charalampakis, M., Sakellariou, D., Flueh, E., Sokos, E., et al. (2016). Slab segmentation controls the interplate slip motion in the SW Hellenic subduction: New insight from the 2008 Mw 6.8 Methoni interplate earthquake. *Geophysical Research Letters, 43*(18), 9619–9626. https://doi.org/10.1002/2016GL070447.

Shaw, B., Ambraseys, N. N., England, P. C., Floyd, M. A., Gorman, G. J., Higham, T. F. G., et al. (2008). Eastern Mediterranean tectonics and tsunami hazard inferred from the AD 365 earthquake. *Nature Geoscience, 1,* 268–276. https://doi.org/10.1038/ngeo151.

Shaw, B., & Jackson, J. (2010). Earthquake mechanisms and active tectonics of the Hellenic subduction zone. *Geophysical Journal International, 181,* 966–984. https://doi.org/10.1111/j.1365-246X.2010.04551.x.

Sodoudi, F., Kind, R., Hatzfeld, D., Priestley, K., Hanka, W., Wylegalla, K., et al. (2006). Lithospheric structure of the Aegean obtained from P and S receiver functions. *Journal of Geophysical Research: Solid Earth.* https://doi.org/10.1029/2005JB003932.

Stein, S., & Wysession, M. (2003). *An introduction to seismology, earthquakes, and earth structure.* Oxford: Blackwell Science. https://doi.org/10.1017/S0016756803318837.

Taymaz, T., Jackson, J., & Westaway, R. (1990). Earthquake mechanisms in the Hellenic Trench near Crete. *Geophysical Journal International, 102,* 695–731. https://doi.org/10.1111/j.1365-246X.1990.tb04590.x.

Wang, H., & Tao, X. (2003). Relationships between moment magnitude and fault parameters: Theoretical and semi-empirical relationships. *Earthquake Engineering and Engineering Vibration, 2,* 201–211.

Watts, P., Grilli, S. T., Kirby, J. T., Fryer, G. J., & Tappin, D. R. (2003). Landslide tsunami case studies using a Boussinesq model and a fully nonlinear tsunami generation model. *Natural Hazards and Earth Systems Sciences, 3,* 391–402.

Wei, G., & Kirby, J. T. (1995). Time-dependent numerical code for extended Boussinesq equations. *Journal of Waterway, Port, Coastal, and Ocean Engineering, 121,* 251–261.

Wei, G., Kirby, J. T., Grilli, S. T., & Subramanya, R. (1995). A fully nonlinear Boussinesq model for surface waves. Part 1. Highly nonlinear unsteady waves. *Journal of Fluid Mechanics, 294,* 71–92.

Wells, D. L., & Coppersmith, K. J. (1994). New empirical relationships among magnitude, rupture length, rupture width, rupture area, and surface displacement. *Bulletin of the Seismological Society of America, 84,* 974–1002.

Wendt, J., Oglesby, D. D., & Geist, E. L. (2009). Tsunamis and splay fault dynamics. *Geophysical Research Letters, 36,* 1. https://doi.org/10.1029/2009GL038295.

Wessel, P., Smith, W. H. F., Scharroo, R., Luis, J., & Wobbe, F. (2013). Generic mapping tools: Improved version released. *Eos, Transactions American Geophysical Union, 94*(45), 409–410.

Yalciner, C.A., Annunziato, A., Papadopoulos, G.A., Guney Dogan, G., Gokhan Guler, H., Eray Cakir, T., Ozer Sozdinler, C., Ulutas, E., Arikawa, T., Suzen, L., Kanoglu, U., Guler, I., Probst, P., & Synolakis, C. (2017). The 20th July 2017 (22:31 UTC) Bodrum/Kos Earthquake and Tsunami; Post Tsunami Field Survey Report.

Zahradnik, J., Sokos, E., & Tselentis, A. (2009). Quick identification of the fault plane for Mw 6.3, earthquake south of Crete, Greece July 1, 2009. Report to EMSC issued on July 1st, 2009 at 20:00 UTC.